Dong *et al.*
Chinese Journal of Mechanical Engineering (2022) 35:35
https://doi.org/10.1186/s10033-022-00689-1

Chinese Journal of Mechanical Engineering

ORIGINAL ARTICLE Open Access

Workspace and Accuracy Analysis on a Novel 6-UCU Bone-attached Parallel Manipulator

Kaijie Dong[1], Duanling Li[1*], Xingyu Xue[1], Chang Xu[2], Haowei Wang[3] and Xianming Gao[4]

Abstract

With the increasingly more extensive application of the medical surgical robot in the clinic, higher requirements have been put forward for medical robots. The bone-attached robot, a popular orthopedic robot in recent years, has a tendency of miniaturization and refinement. Thus, a bone-attached parallel manipulator (PM) based on 6-UCU (universal-cylindrical-universal) configuration is proposed, which is characterized by small volume, compact structure, high precision and six-dimensional force feedback. To optimize the structure and make it more compact, the workspace of the 6-UCU PM is analyzed based on the analysis of three kinds of constraint, and workspace model is established through spherical coordinate search method. This study also analyzes the influence of structural parameters on workspace, which may contribute to improving the efficiency of design and ensuring small-sized robots possess relatively large workspace. Moreover, to improve the motion accuracy, an error modeling method is developed based on the structure of 6-UCU PMs. According to this established error model, the output pose error curves are drawn using MATLAB software when the structure parameters change, and the influence of the structure and pose parameters change on the output pose error of PMs is analyzed. The proposed research provides the instruction to design and analysis of small PMs such as bone-attached robots.

Keywords: Medical robot, Bone-attached robot, Parallel manipulator, Workspace analysis, Accuracy analysis

1 Introduction

With the rapid development of mechanism, computer science, automatic control, artificial intelligence and other disciplines, robotics has made great progress, and its application field has become more and more broad. In the 1980s, robots began to be introduced into the robot-assisted surgical system, and have gradually developed from the early industrial robots to special surgical robots [1]. After decades of continuous innovation and development, the surgical robot has shown its unique technical advantages. It could lead to a revolutionary surgical mode and the development of minimally invasive operation [2, 3]. Research and clinical studies have reported significant improvement in outcomes of surgical operations [4], including a reduction in trauma experienced by patients and post-procedure recovery of patients [5, 6], such as,by 2018, Da Vinci® surgical robots had performed about 1.03 million surgeries [7]; TiRobot®, a versatile orthopedic robot, has been widely used in clinical surgery [8, 9], greatly simplifying the surgical process and reducing patient pain.

Orthopedic robot is a branch of medical robot field, which originated in the early 1990s [4, 6]. The first known active robot introduced to the operating room was the Robodoc system. This robot is used to mill the medullary cavity of the femur for a cementless femoral prosthesis in total hip replacement and the first total hip arthroplasty was completed in 1992. Another application of the Robodoc system is presented by Kazanzides et al. [10] where the robot actively mills the femur in order to optimally fit an implant for knee surgery. With the continuous deepening of research, more and more special orthopedic surgical robots are starting

*Correspondence: liduanling_bupt@163.com
[1] School of Automation, Beijing University of Posts and Telecommunications, Beijing 100876, China
Full list of author information is available at the end of the article

to show up. Meanwhile, due to the advantages of high stiffness, compact structure, high accuracy and robustness [1, 11], PM is used in the research of orthopedic surgery system, in which many PMs arise.

As for total knee replacement, Imperial College London developed an Acrobot system [12], which is shown in Figure 1. It systematically combines the surgical image with the physical prosthesis model, and implement the path planning in the scanned three-dimensional CT image. And then, schematization and simulation are also carried out in the physical model [12, 13]. According to the operation area to be operated, the relevant operation is carried out, which can predict and verify the operation in advance, and improve the accuracy of the operation.

Making use of the advantage of a PM structure, a novel semi-active medical robotic concept was introduced by Wolf and Shoham et al. [14, 15], which is shown in Figure 2. In this work, they introduced a concept of a miniature bone-attached PM. Taking advantage of a PM's attributes such as low weight, high accuracy, and compactness, they introduced the concept of a miniature, low mass, bone attached PM specially designed for spinal operations.

As shown in Figure 3, Renaissance® system, a 6-DOF miniature PM system, was introduced by an Israel company called Mazor Surgical Technologies [16–18]. It adopts the "Hover-T" technology, which can be directly fixed on the patient's spine and guide the operators to carry out internal fixation. The Renaissance system has been certified by FDA and CE, and according to clinical reports, the accuracy rate of screw placement was 98.5%, which was significantly better than the traditional operation. However, there exist some defects such as complex operation and lack of real-time image monitoring.

According to the existing research, the bone-attached robot usually needs a smaller volume to avoid occupying a larger operation space; meanwhile, high accuracy is required for accurate positioning; better stiffness and larger bearing capacity are also required to meet the needs of milling, guiding and other orthopedic operations. Moreover, in order to improve the safety of the operation process, force feedback should be added to the bone-attached robot, so that it can detect the mechanical signal in real time, identify the abnormal signal and give an alarm. Therefore, a novel 6-UCU bone-attached PM is proposed, considering low weight, compact structure, high accuracy, high stiffness, restricted workspace, high frequency response and low cost respectively.

Figure 1 Acrobot [12]

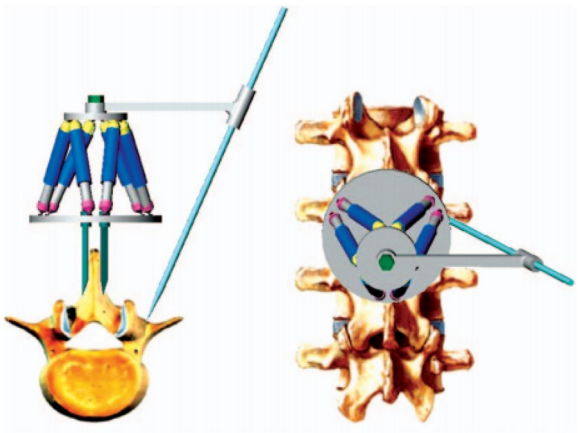

Figure 2 Bone-attached PM [14]

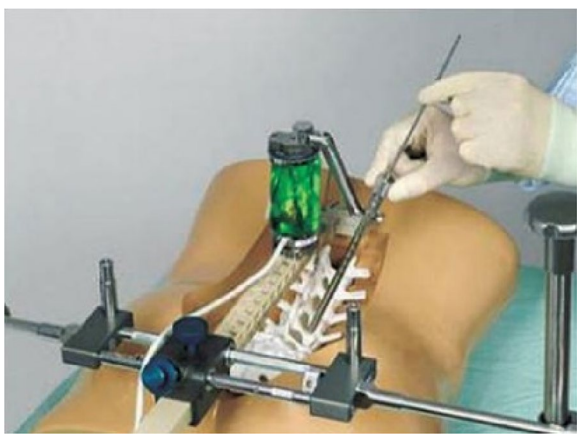

Figure 3 Mazor Renaissance® [16]

To better optimize the structure and obtain higher accuracy, the motion space and the influencing factors of accuracy of the 6-UCU PM is analyzed in this paper. The rest of this paper is organized as follows. Section 2 introduces the design of a 6-UCU PM in detail, including the design of the UCU limb and the description of the 6-UCU parallel mechanism. Section 3 analyses the workspace of PM. Section 4 analyses the influence of structure parameters on output pose accuracy. Section 5 concludes this paper.

2 6-UCU Bone-attached PM

Due to the simple structure and perfect theoretical research, the 6-UPS (universal-prismatic-spherical) parallel mechanism is a widely used type of PM. However, as a result of the difficulty and high cost of the manufacturing of small-size spherical joint, a small 6-UCU PM is proposed based on the structure of 6-UPS parallel mechanism. The PM presented in this paper consists of a moving platform, a base and six identical limbs. Hooke joints are respectively used to connect the fixed base with the limbs and the limbs with the moving platform, and the structure of which is shown in Figure 4(a). Figure 4(b) presents the prototype of 6-UCU PM. In the initial state, the height of the PM is 120 mm, and the radiuses of the moving platform and the fixed base are 50 mm.

According to the screw theory, the degree of freedom of the parallel mechanism is analyzed. It is easy to know that in a UCU limb, the U pair has two rotational degrees of freedom, and the two rotational axes intersect at a point. The C pair has two degrees of freedom—translational movement and rotation along the axis. When the axis of C pair passes the intersection point of the axes of any U pairs, the twist screw of a UCU limb is a 6-system. Therefore, the 6-UCU parallel platform also has six degrees of freedom. The motion of the cylindrical pair is driving motion, and the other pairs are driven motion. The pose of the parallel mechanism is realized by changing the length of the limbs.

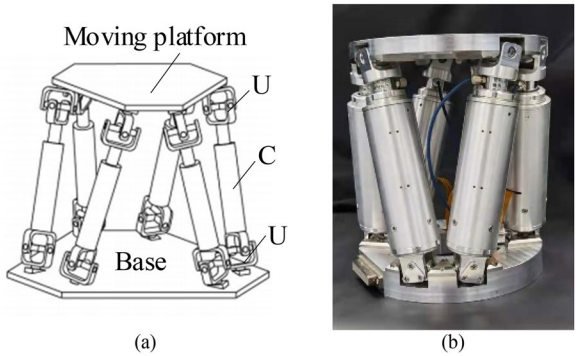

Figure 4 6-UCU bone-attached PM: **a** 6-UCU parallel mechanism, **b** Prototype of the 6-UCU bone-attached PM

2.1 Design of the UCU Limb

Due to the mechanical structure of PM, it can be obtained that driving link is one of the most important parts in PMs, and it's the basis of the normal operation of PM. The structure of driving link is shown in Figure 5, including two Hooke joints (U pairs), an ultrasonic motor, a micro precision encoder, a lead screw and a bearing. There exists a R pair between the nut and the sleeve though the bearing, which forms a cylindrical pair together with the screw. The axis of the R pair intersects with the axes of the Hooke joint at the center point, it can be equivalent to a spherical joint, as shown in Figure 6. The configuration of the 6-UCU parallel mechanism can be equivalent to a 6-UPS parallel mechanism.

The equivalent spherical joint and Hooke joint are connected with the base and moving platform respectively to provide enough freedom for the motion of the PM. The Ultrasonic motor is the power source to drive the link. Compared with the traditional motor, the ultrasonic motor has the advantages of larger torque to weight ratio, compact structure and not affected by the magnetic field. In addition, the ultrasonic motor has the characteristics of low noise, high resolution, simple control, fast response, various shapes, and can work normally in complex environment. Micro precision encoder is used to detect and provide feedback to the rotation angle of ultrasonic motor and the position of lead screw, which is the key to realize the accuracy and error compensation.

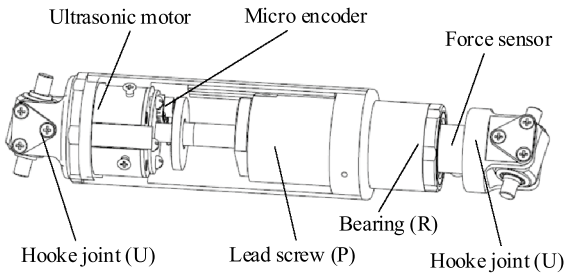

Figure 5 Structure of the UCU chain

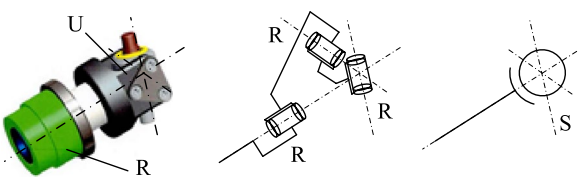

Figure 6 Equivalent spherical joint

The lead screw converts the rotation output of the ultrasonic motor into a linear output to complete the expansion and contraction of the driving link. The above hardware is the key to ensure the 6-UCU PM has high accuracy and large bearing capacity. The force sensor is used to detect the pressure of each branch chain, and the six axis force of the moving platform can be obtained through calculation, which is convenient for real-time detection of the force during operation and improves the safety of the bone-attached robot.

2.2 Description of the PM

A 6-UCU parallel mechanism consists of a manipulator and 6 limbs evenly distributed around the manipulator, as shown in Figure 7. The Hooke joints on the moving platform are divided into three groups and evenly distributed on the circumference with radius R, the angle corresponding to the two joint points in each group is α; The Hooke joints on the base are divided into three groups, and the groups evenly distributed on the circle with radius R_0. The angle corresponding to the two joint points in each group is β.

The homogeneous transformation matrix $\boldsymbol{T}$ from the moving platform coordinate system *O-XYZ* to the body coordinate system O_0-$X_0Y_0Z_0$ can be denoted as:

$$\boldsymbol{T} = \begin{bmatrix} \boldsymbol{R} & \boldsymbol{P} \\ \boldsymbol{o} & 1 \end{bmatrix}, \tag{1}$$

where, the 3×1 matrix $\boldsymbol{P} = [X_p\ Y_p\ Z_p]^{\mathrm{T}}$ denotes translation, and the $\boldsymbol{R}$ is rotation matrix, each column of which is the direction cosine of *X*, *Y*, *Z* in the coordinate system *O-XYZ*.

$$\boldsymbol{R} = \begin{bmatrix} l_1 & m_1 & n_1 \\ l_2 & m_2 & n_2 \\ l_3 & m_3 & n_3 \end{bmatrix}. \tag{2}$$

According to the vector expression of each link of the mechanism, we can obtain:

$$l_i \boldsymbol{n}_i = \boldsymbol{P} + \boldsymbol{R} \cdot \boldsymbol{a}_i - \boldsymbol{b}_i, \ \ i = 1 - 6, \tag{3}$$

where l_i is the length of the link *i*, $\boldsymbol{n}_i$ is the unit vector of the link a_ib_i. The direction of the vector is from the hinge point $\boldsymbol{a}_i$ to the hinge point $\boldsymbol{b}_i$.

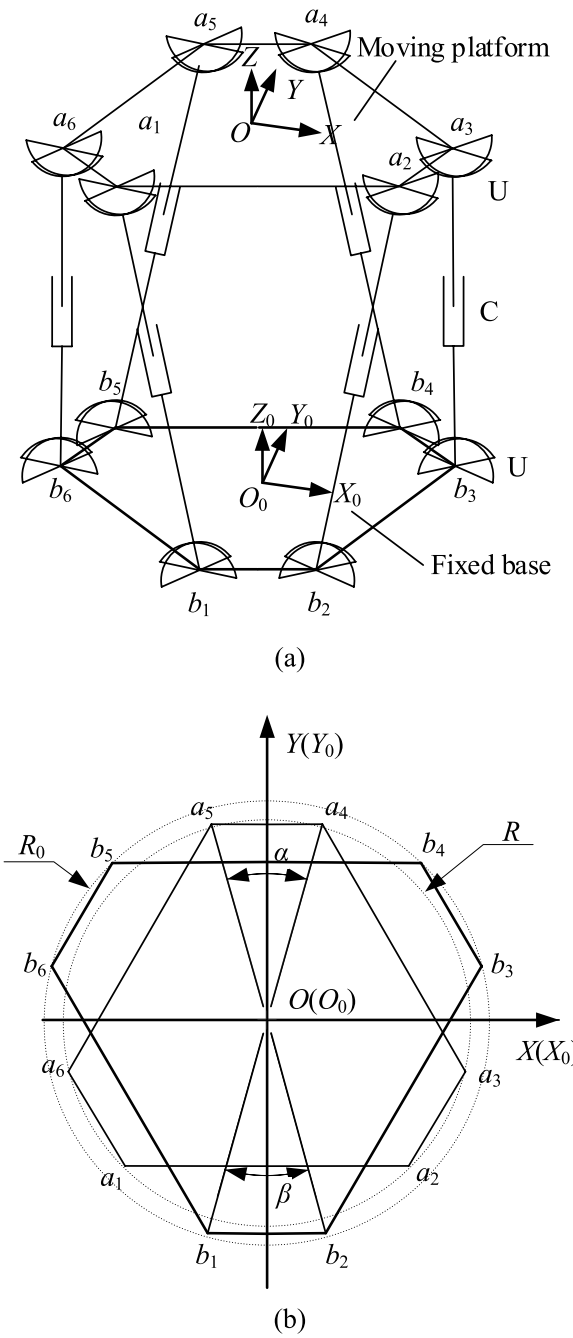

Figure 7 Coordinate and setting of the 6-UCU parallel mechanism: **a** Kinematic diagram, **b** Distribution map of joints

3 Workspace Analysis of PM

The workspace of a PM is the set of all the working areas that the reference points on the moving platform can reach. It is an important parameter to measure the working performance of the PM. The shape and size of the working area determine the motion ability of the PM. Compared with serial mechanisms, the workspace of PMs is generally smaller and the shape is irregular, which limits the application range of PMs. Therefore, analysis of workspace is a key segment in the design of PMs.

Workspace analysis of PM is usually the process of solving its maximum workspace, the calculation process of the workspace of PM is generally very complex, the current solution methods include numerical solution and analytical solution. The geometric solution method

proposed by Jo and developed by Gosselin is the most representative analytical solution [11, 19]. Based on CAD software, Arrouk [20] obtained the calculation of workspace of PM by calculating the intersection of simple 3D geometry. Xiong et al. [21] analyzed geometric isotropy indices for workspace. Fu et al. [22] and Antonov et al. [23] explore the dependence of the workspaces on the manipulator geometric parameters. The numerical solution of the workspace of PM is to use the inverse position solution to calculate the parameters such as the joint angle and the length of the link under the given posture. By comparing with the constraint conditions, it can judge whether the given posture can be reached, so as to determine the range of the workspace [24–26]. In this paper, the workspace of the designed PM is analyzed by using the numerical method of searching the workspace limit boundary.

3.1 Limitation of the Length of Links

There are many limiting factors of solving workspace. In which there are three main influencing factors: the limitation of the length of each driving link, the limitation of the rotation angle of each pair and the interference between the driving links.

According to Eq. (3), the length of each link l_i can be expressed as follows:

$$l_i = |\boldsymbol{P} + \boldsymbol{R} \cdot \boldsymbol{a}_i - \boldsymbol{b}_i|, i = 1 - 6. \tag{4}$$

If $l_{i\,\min}$ is the shortest length of the link l_i and $l_{i\,\max}$ is the longest length of the link i, the following constraints in the actual motion process can be expressed as follows:

$$l_{i\,\min} \le l_i \le l_{i\,\max}, i = 1 - 6. \tag{5}$$

Whenever the length of any link reaches its limit, the reference point on the moving platform reaches the limit boundary of its workspace.

3.2 Limitation of the Rotation Angle of Kinematic Pair

The equivalent spherical joint (U-R) is used between the moving platform and the driving link, and the Hooke joint is used between the base and the driving link. The equivalent spherical joint is three independent rotation pairs, and the diagram of the equivalent spherical joint is shown in Figure 8.

In the PM analyzed in this paper, the angles θ_1, θ_2 and θ_3 are limited by the structural parameters and constraints of the PM, and range of their changes can be expressed as follows:

$$\theta_i \le \theta_{i\,\max}, \quad i = 1 - 3, \tag{6}$$

where $\theta_{i\,\max}$ is the maximum limitation angle of each pair.

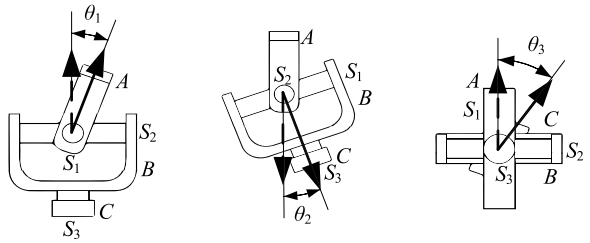

Figure 8 Diagram of the equivalent spherical joint

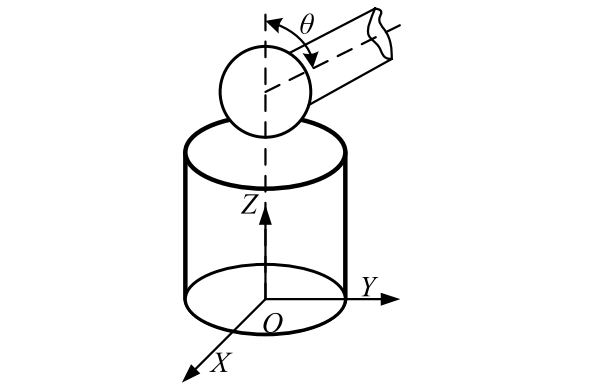

Figure 9 Rotation angle of spherical kinematic pair

For the convenience of calculation, the three rotation angles of the equivalent spherical joint are simplified as the rotation angle θ of the spherical joint, which is shown in Figure 9. The rotation angle θ of the spherical pair is determined by the Z axis of the moving coordinate system and the vector $\boldsymbol{u}$ of the link, and its limitation value is the minimum value of $\theta_{i\,\max}$. Similarly, the rotation angles of Hooke joint also have a range.

Vector $\boldsymbol{n}_{ai}$ denotes the posture of the base of spherical pair on the moving platform in the moving coordinate system O-XYZ, and vector $\boldsymbol{n}_{bi}$ denotes the posture of the base of the Hooke joint in the base coordinate system O_0-$X_0Y_0Z_0$. θ_{ai} is the rotation angle of spherical pair, θ_{bi} is the rotation angle of Hooke joint, as shown in Figure 10.

Then the constraint condition of the spherical pair can be expressed as:

$$\theta_{ai} = \arccos \frac{\boldsymbol{L}_i \cdot (\boldsymbol{R}\boldsymbol{n}_{ai})}{|\boldsymbol{L}_i|} \le \theta_{a\,\max}, \quad i = 1 - 6, \tag{7}$$

where $\boldsymbol{L}_i$ is the vector between two pairs of the ith link. The constraint condition of the Hooke joint can be expressed as:

$$\theta_{bi} = \arccos \frac{\boldsymbol{L}_i \cdot (\boldsymbol{R}\boldsymbol{n}_{bi})}{|\boldsymbol{L}_i|} \le \theta_{b\,\max}, \quad i = 1 - 6. \tag{8}$$

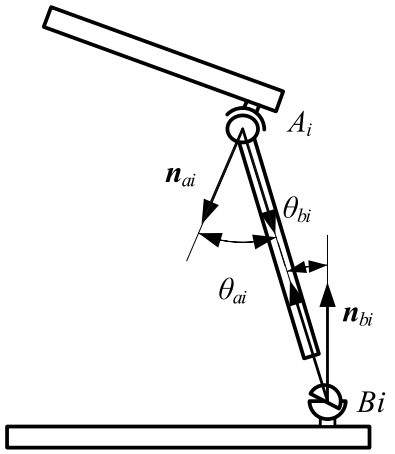

Figure 10 Setting of the rotation angle

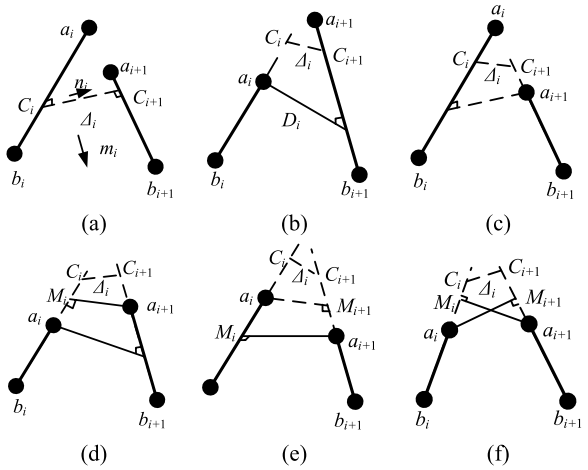

Figure 11 Interference cases of links

3.3 Interference of Link

The possible interference between the moving platform, the base and the driving link should be considered in the motion of PM due to the certain physical dimensions there all exist. Suppose that each link in the PM is a standard cylinder, of which D denotes the diameter of the link and D_i denotes the distance between central axis of adjacent links. Therefore, the constraint condition of interference between links can be expressed as

$$D \le D_i, \quad i = 1 - 6, \tag{9}$$

where $\boldsymbol{n}_i$ denotes the unit vector of the common normal between the adjacent link vectors $\boldsymbol{L}_i$ and $\boldsymbol{L}_{i+1}$:

$$\boldsymbol{n}_i = \frac{\boldsymbol{L}_i \times \boldsymbol{L}_{i+1}}{|\boldsymbol{L}_i \times \boldsymbol{L}_{i+1}|}, \tag{10}$$

where Δ_i denotes the minimum distance between the vectors $\boldsymbol{L}_i$ and $\boldsymbol{L}_{i+1}$:

$$\Delta_i = |\boldsymbol{n}_i \cdot (\boldsymbol{b}_{i+1} - \boldsymbol{b}_i)|. \tag{11}$$

The relationship between the minimum distance Δ_i and the distance D_i depends on the positions of the common normal intersections C_i and C_{i+1}, The coordinates $\boldsymbol{c}_i$ of intersection C_i can be calculated by Eq. (9):

$$\frac{\boldsymbol{c}_i - \boldsymbol{b}_i}{\boldsymbol{a}_i - \boldsymbol{b}_i} = \left| \frac{(\boldsymbol{b}_{i+1} - \boldsymbol{b}_i) \cdot \boldsymbol{m}_i}{(\boldsymbol{a}_i - \boldsymbol{b}_i) \cdot \boldsymbol{m}_i} \right|, \tag{12}$$

where $\boldsymbol{a}_i$ denotes the coordinates of joints a_i in base coordinate system O_0-$x_0y_0z_0$, $\boldsymbol{m}_i$ can be expressed as:

$$\boldsymbol{m}_i = \boldsymbol{n}_i \times (\boldsymbol{a}_{i+1} - \boldsymbol{b}_{i+1}). \tag{13}$$

Similarly, $\boldsymbol{c}_{i+1}$ can be calculated. According to the position of the intersection points C_i and C_{i+1} on the link, there are three cases:

(1) The intersections C_i and C_{i+1} are both on the link, shown as Figure 11(a). The interference condition of links under this circumstance can be expressed as $\Delta_i > D$.

(2) If the intersection point C_i or C_{i+1} is not on the link, as shown in Figure 11(b) and (c), D_i is calculated according to the position of C_i or C_{i+1}. If C_{i+1} is on link $a_{i+1}b_{i+1}$, D_i is the distance from a_i to link $a_{i+1}b_{i+1}$:

$$D_i = \left| \frac{(\boldsymbol{a}_i - \boldsymbol{b}_{i+1}) \times \boldsymbol{L}_{i+1}}{\boldsymbol{L}_{i+1}} \right|. \tag{14}$$

If C_{i+1} is on link a_ib_i, as shown in Figure 11(c), D_i is the distance from a_{i+1} to link a_ib_i:

$$D_i = \left| \frac{(\boldsymbol{a}_{i+1} - \boldsymbol{b}_i) \times \boldsymbol{L}_i}{\boldsymbol{L}_i} \right|, \tag{15}$$

(3) If the intersection points C_i or C_{i+1} are not on the link, as shown in Figure 11(d)–(f), D_i depends on the positions of M_i and M_{i+1}, where, M_i is the intersection of the line passing through the joint point a_{i+1} and perpendicular to $\boldsymbol{L}_i$ and $\boldsymbol{L}_{i+1}$, and M_{i+1} is the intersection of the line passing through the joint point and perpendicular to L_i and L_{i+1}. Under this condition, there are three possibilities as follows:

As shown in Figure 11(d), when M_i is outside the link a_ib_i and M_1 is on the link $a_{i+1}b_{i+1}$, D_i can be obtained by Eq. (14); As shown in Figure 11(e), when M_i is on the link a_ib_i and M_1 is outside the link $a_{i+1}b_{i+1}$, D_i can be obtained by Eq. (15); As shown in Figure 11(f), when M_i and M_1 are both outside the links, D_i is the distance from a_i to link $a_{i+1}b_{i+1}$.

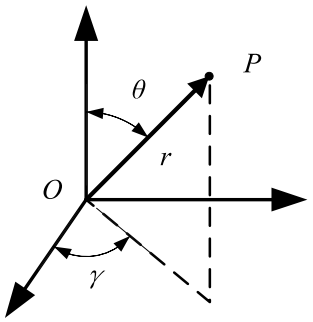

Figure 12 Setting of the spherical coordinate

3.4 Calculation on Workspace

3.4.1 Spherical Coordinate Searching Method

The spherical coordinate searching method is to express any point $\boldsymbol{P} = [X_p\ Y_p\ Z_p]^{\mathrm{T}}$ in space by establishing spherical coordinate system. The radial distance ρ represents the distance from the target point P to the origin O of the coordinate system, the zenith angle ϕ represents the angle between the line OP and the positive direction of the Z axis, and the azimuth Φ represents the deflection angle of the line OP relative to the XZ plane, as shown in Figure 12.

The specific steps of calculation on workspace boundary are shown in Figure 13. Firstly, the initial pose and structural parameters of the PM are acquired according to the requirements of this subject. The components X_P, Y_P and Z_P of point P are expressed in spherical coordinates. Maintain the zenith angle ϕ and increase the azimuth Φ from 0 to 2 π, the maximum radial distance $P_{\max}$ is found according to the kinematic theory and constraint conditions of PM. Gradually, increase the Zenith angle from 0 to π, according to the previous steps to find out the maximum radial distance $P_{\max}$.

3.4.2 Influence of Structural Parameters on Workspace

The workspace of the PM can be obtained by the spherical coordinate searching method. The structure parameters of PM are related to radius R, circle angle α, radius R_0 and circle angle β. And in former analysis we have $\alpha=\beta$ and $R=R_0$. In order to analyze the influence of the structure parameters on the workspace, the influence of the four parameters on the workspace is analyzed.

Figure 14(a) shows the workspaces of PM with the radius R ($R=R_0$) of 50 mm, 55 mm and 60 mm. It can be obtained that when the angle α and β and other constraints remain unchanged, the workspace size within a certain range decreases with the increase of radius R and R_0. It can be obtained from Figure 14(b) that under the condition that radius R (R_0) is 50 mm and other constraints remain unchanged, with the increase of circumference angle α and β with the increase of the value, the workspace of the PM is increasing.

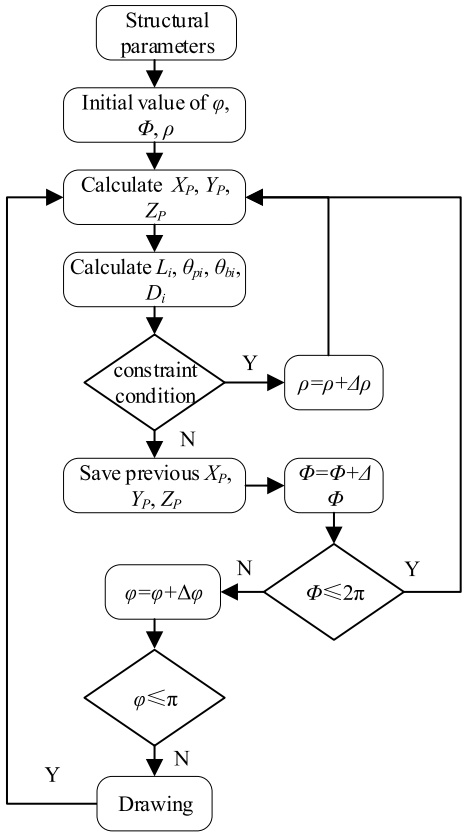

Figure 13 Calculation flow chart

3.4.3 Presentation of Workspace

According to the spherical coordinate searching method, the workspace of the PM is searched and drawn by using MATLAB software. What in Figure 15 signifies the workspace of the PM. Figure 15(a) is a 3D view of the workspace of the PM. Figure 15(b) is the projection of the workspace in XY plane. Figure 15(c) is the projection of the workspace in XZ plane.

It can be acquired from Figure 15 that the workspace of the PM basically presents a relatively regular shape, and the working range of the reference point of the PM in the X axis direction is within ±30 mm. The working range of the reference point in the Y axis direction is about −35 mm and +30 mm, and the working range of the reference point in the Z axis direction is about 120 mm and 150 mm, which fully meets the design requirements.

In order to calculate the obliquity of the PM in X, Y, Z directions, which also means to solve the maximum

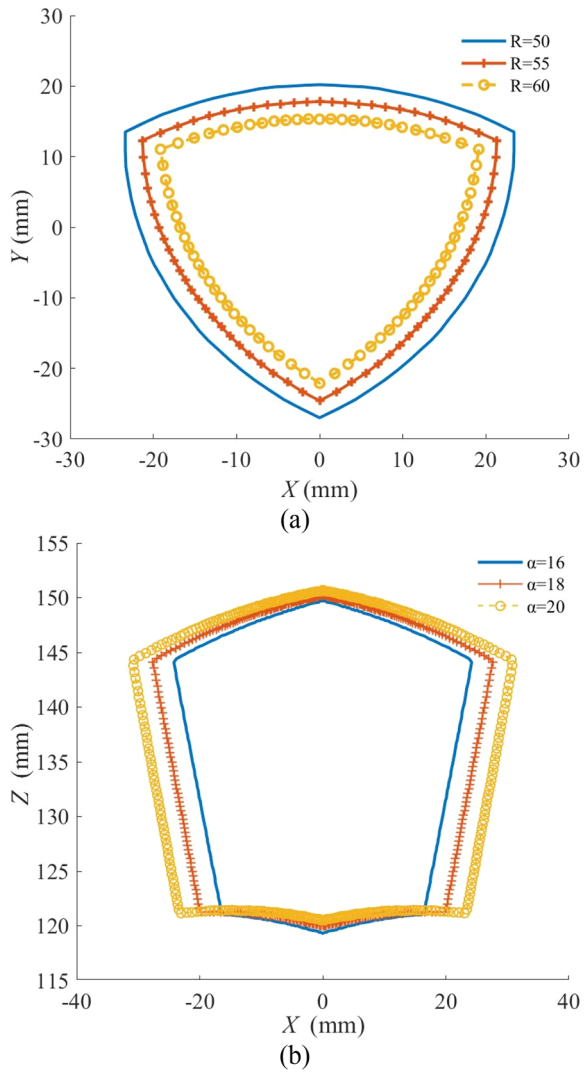

Figure 14 Influence of structural parameters on workspace: R and R_o, a and β

and minimum values of the three pose angles ϕ, θ, γ in the workspace, the curve of the pose angle is shown in Figure 16. As shown in Figure 16, the inclination angle range in X direction is from $-27°$ to 27.79°, the inclination angle range in Y direction is from $-8.76°$ to 8.76°, the inclination angle range in Z direction is from $-10.37°$ to 8.43°.

4 Accuracy Analysis of PM

Accuracy analysis is the basis of the accuracy research of PMs. By establishing the error model of PMs, the influence of various error factors on the pose error of PMs is analyzed [27, 28].

In this section, we present a digital error model based on the relationship between the structural parameter error and the output pose error of the PMs, which is established by using the differential method of the vector equation of the link [29, 30], to analyze the influence of structural parameter error on output pose error of PMs.

4.1 Error Modeling

Considering the working accuracy and assembly errors, the total differential calculation of Eq. (3) is required [25], the result is

$$\mathrm{d}l_i\boldsymbol{n}_i + l_i\mathrm{d}\boldsymbol{n}_i = \mathrm{d}\boldsymbol{P} + \mathrm{d}\boldsymbol{R}\cdot\boldsymbol{a}_i + \boldsymbol{R}\cdot\mathrm{d}\boldsymbol{a}_i - \mathrm{d}\boldsymbol{b}_i, \tag{16}$$

where

$$\mathrm{d}\boldsymbol{n}_i = \begin{bmatrix} 0 & -\delta n_{iz} & \delta n_{iy} \\ \delta n_{iz} & 0 & -\delta n_{ix} \\ -\delta n_{iy} & \delta n_{ix} & 0 \end{bmatrix}, \tag{17}$$

From the perturbation matrix [26] of the rotation matrix $\boldsymbol{R}$, we can obtain

$$\mathrm{d}\boldsymbol{R} = \begin{bmatrix} 0 & -\delta\theta_z & \delta\theta_y \\ \delta\theta_z & 0 & -\delta\theta_x \\ -\delta\theta_y & \delta\theta_x & 0 \end{bmatrix}\cdot\boldsymbol{R} = \Delta\boldsymbol{R}\cdot\boldsymbol{R}, \tag{18}$$

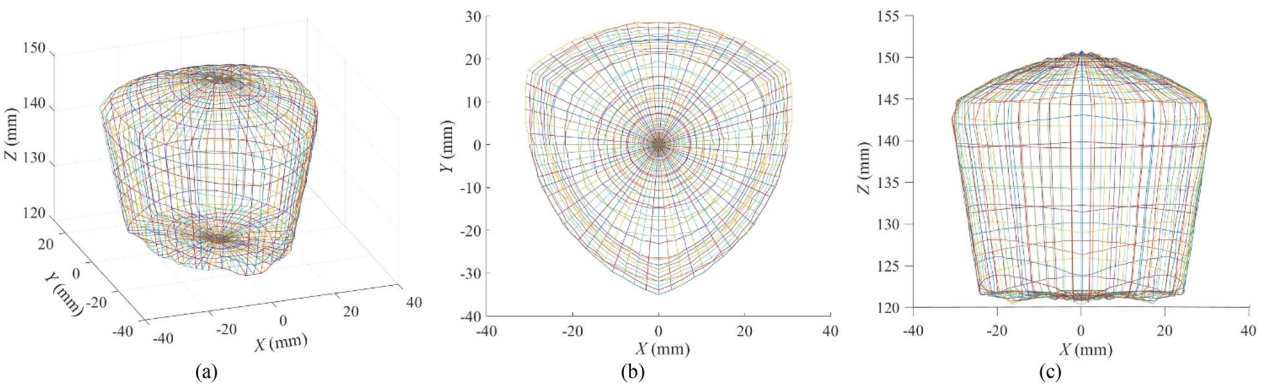

Figure 15 Workspace of the PM: **a** 3D view of the workspace, **b** Workspace in XY plane, **c** Workspace in XZ plane

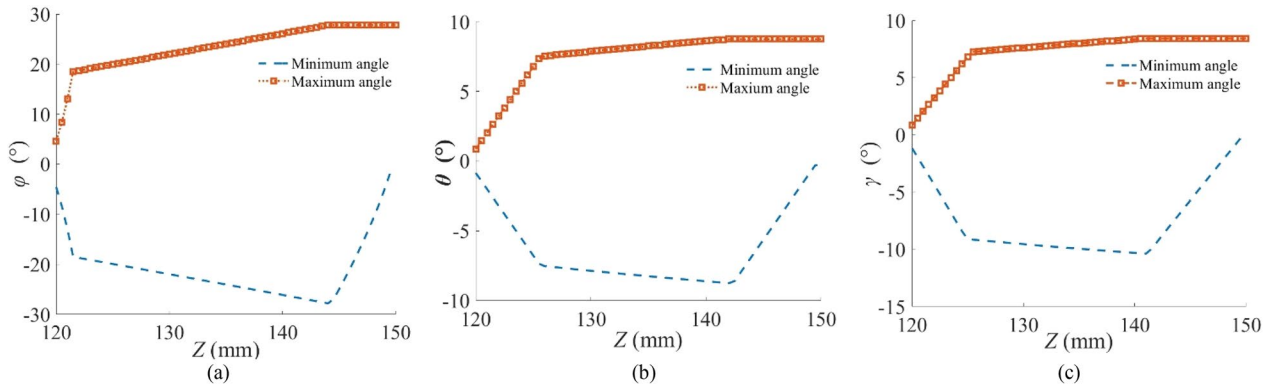

Figure 16 Pose angle to *Z*: **a** φ to *Z*, **b** θ to *Z*, **c** γ to *Z*

where $\delta\theta_x$, $\delta\theta_y$, $\delta\theta_z$ is the position error vector of the moving platform, the posture error component is denoted as $\delta\boldsymbol{\theta} = \left[\begin{array}{ccc}\delta\theta_x & \delta\theta_y & \delta\theta_z\end{array}\right]^{\mathrm{T}}$.

By multiplying $\boldsymbol{n}_i^{\mathrm{T}}$ to both ends of Eq. (18), we can get

$$\boldsymbol{n}_i^{\mathrm{T}}\mathrm{d}l_i\boldsymbol{n}_i + \boldsymbol{n}_i^{\mathrm{T}}l_i\mathrm{d}\boldsymbol{n}_i = \boldsymbol{n}_i^{\mathrm{T}}\mathrm{d}\boldsymbol{P} + \boldsymbol{n}_i^{\mathrm{T}}\mathrm{d}\boldsymbol{R}\cdot\boldsymbol{a}_i + \boldsymbol{n}_i^{\mathrm{T}}\boldsymbol{R}\cdot\mathrm{d}\boldsymbol{a}_i - \boldsymbol{n}_i^{\mathrm{T}}\mathrm{d}\boldsymbol{b}_i, \tag{19}$$

Since $\boldsymbol{n}_i^{\mathrm{T}}\boldsymbol{n}_i = 1$ and $\boldsymbol{n}_i^{\mathrm{T}}\cdot\mathrm{d}\boldsymbol{n}_i = 0$, Eq. (19) can be expressed as:

$$\mathrm{d}l_i = \boldsymbol{n}_i^{\mathrm{T}}\mathrm{d}\boldsymbol{P} + (\boldsymbol{n}_i^{\mathrm{T}}\delta\boldsymbol{\theta})\times(\boldsymbol{R}\boldsymbol{a}_i) + \boldsymbol{n}_i^{\mathrm{T}}\boldsymbol{R}\cdot\mathrm{d}\boldsymbol{a}_i - \boldsymbol{n}_i^{\mathrm{T}}\mathrm{d}\boldsymbol{b}_i. \tag{20}$$

Assuming $\delta\boldsymbol{P} = \mathrm{d}\boldsymbol{P}$, $\delta l_i = \mathrm{d}l_i$, $\delta\boldsymbol{a}_i = \mathrm{d}\boldsymbol{a}_i$, $\delta\boldsymbol{b}_i = \mathrm{d}\boldsymbol{b}_i$, Eq. (20) can be expressed as:

$$\delta l_i = \left[\begin{array}{cc}\boldsymbol{n}_i^{\mathrm{T}} & \boldsymbol{n}_i^{\mathrm{T}}\times(\boldsymbol{R}\boldsymbol{a}_i)\end{array}\right]\cdot\left[\begin{array}{c}\delta\boldsymbol{P}\\ \delta\boldsymbol{\theta}\end{array}\right] + \left[\begin{array}{cc}\boldsymbol{n}_i^{\mathrm{T}}\boldsymbol{R} & -\boldsymbol{n}_i^{\mathrm{T}}\end{array}\right]\cdot\left[\begin{array}{c}\delta\boldsymbol{a}_i\\ \delta\boldsymbol{b}_i\end{array}\right]. \tag{21}$$

Integrating the formulas of the six links, the following can be obtained:

$$\delta\boldsymbol{l} = \boldsymbol{J}_1\cdot\delta\boldsymbol{M} + \boldsymbol{J}_2\cdot\delta\boldsymbol{K}. \tag{22}$$

Among Eq. (22), where

$$\delta\boldsymbol{l} = \left[\begin{array}{cccccc}\delta l_1 & \delta l_2 & \delta l_3 & \delta l_4 & \delta l_5 & \delta l_6\end{array}\right]^{\mathrm{T}},$$

$$\boldsymbol{J}_1 = \left[\begin{array}{cc}\boldsymbol{n}_1^{\mathrm{T}} & \boldsymbol{n}_1^{\mathrm{T}}\times(\boldsymbol{R}\boldsymbol{a}_1)\\ \vdots & \vdots\\ \boldsymbol{n}_6^{\mathrm{T}} & \boldsymbol{n}_6^{\mathrm{T}}\times(\boldsymbol{R}\boldsymbol{a}_6)\end{array}\right],$$

$$\delta\boldsymbol{M} = \left[\begin{array}{c}\delta\boldsymbol{P}\\ \delta\boldsymbol{\theta}\end{array}\right]\in R^{6\times1},$$

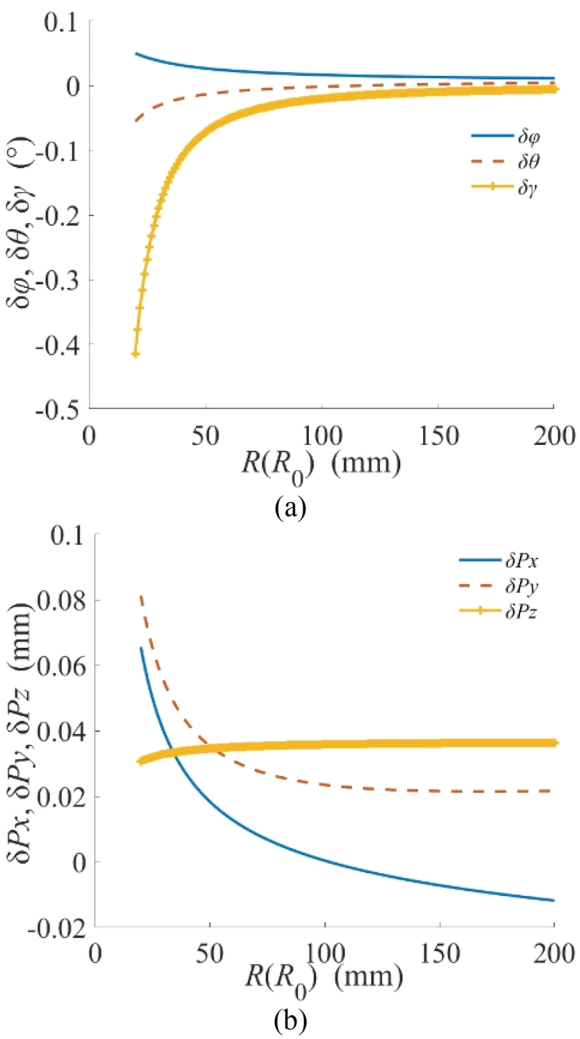

Figure 17 Relation between radius $R(R_0)$ and output pose errors: **a** δP_x, δP_y, δP_z to $R(R_0)$, **b** $\delta\varphi$, $\delta\theta$, $\delta\gamma$ to $R(R_0)$

Table 1 Parameter settings (mm)

Number	1	2	3	4	5	6
a_{xi}	−13.78	13.78	48.51	34.73	−34.73	−48.51
a_{yi}	−48.06	−48.06	12.10	35.97	35.97	12.10
b_{xi}	−34.73	34.73	48.51	13.78	−13.78	−48.51
b_{yi}	−35.97	−35.97	−12.10	48.06	48.06	−12.10

Table 2 Structural error of PM (mm)

No.	δa_{ix}	δa_{iy}	δa_{iz}	δb_{ix}	δb_{iy}	δb_{iz}	δl_i
1	−0.02	0.02	−0.01	−0.01	−0.01	0.02	0.01
2	0.01	0.02	0.02	−0.01	−0.01	0.02	0.02
3	−0.01	−0.01	0.01	−0.03	0.01	0.02	0.02
4	0.02	0.02	0.02	−0.01	−0.01	0.02	−0.01
5	−0.01	0.02	−0.02	−0.01	0.01	0.02	−0.01
6	0.01	0.03	0.01	−0.01	−0.01	0.02	0.02

Table 3 Output pose error of PM

δP_x (mm)	δP_y (mm)	δP_z (mm)	$\Delta\varphi$ (°)	$\Delta\theta$ (°)	$\Delta\gamma$ (°)
0.0184	0.0354	0.0346	0.0267	−0.0135	−0.0722

$$\boldsymbol{J}_2 = \begin{bmatrix} \boldsymbol{n}_1^{\mathrm{T}}\boldsymbol{R} & -\boldsymbol{n}_1^{\mathrm{T}} & \cdots & 0 & 0 \\ \vdots & \vdots & \ddots & \vdots & \vdots \\ 0 & 0 & \cdots & \boldsymbol{n}_6^{\mathrm{T}}\boldsymbol{R} & \boldsymbol{n}_6^{\mathrm{T}} \end{bmatrix},$$

$$\delta\boldsymbol{K} = \begin{bmatrix} \delta\boldsymbol{a}_i \\ \delta\boldsymbol{b}_i \end{bmatrix} \in R^{36\times 1}.$$

Since the inverse matrix of $\boldsymbol{J}_1$ can be obtained, Eq. (22) can be expressed as:

$$\delta\boldsymbol{M} = \boldsymbol{J}_1^{-1}\delta\boldsymbol{l} - \boldsymbol{J}_1^{-1}\boldsymbol{J}_2 \cdot \delta\boldsymbol{K}. \tag{23}$$

Through Eq. (23), the influence of joint error and link input error on the output pose error of the moving platform of the PMs can be obtained.

4.2 Case Study and Error Parameter Analysis

4.2.1 Method Verification

An example of the 6-UCU parallel mechanism is used to analyze the proposed accuracy analysis method. The parameter settings are presented as shown in Table 1.

Assuming the pose parameters are presented as follows:

$$\boldsymbol{P} = \begin{bmatrix} 5 & 5 & 120 \end{bmatrix}^{\mathrm{T}},$$

$$\boldsymbol{R} = \begin{bmatrix} 0.9948 & -0.0493 & 0.0888 \\ 0.0521 & 0.9982 & -0.0303 \\ -0.0872 & 0.0348 & 0.9956 \end{bmatrix}.$$

Structural error is shown in Table 2.

According to the accuracy analysis, the pose error of the PMs is shown in Table 3.

4.2.2 Influence of Structural and Pose Parameters on Output Pose Accuracy

By analyzing the error model, it can be obtained that the values of the structure parameters of the PMs affect the accuracy of the output pose of the PMs.

According to the coordinate and parameter setting of PMs, the structure parameters of PMs are related to radius R, circle angle α, radius R_0 and circle angle β. And in former analysis we have α=β and R=R_0. Assuming the output pose of PM $\boldsymbol{P}$=[5 5 120]$^{\mathrm{T}}$ and $\boldsymbol{\omega}$=[3 2 2]$^{\mathrm{T}}$, the influence of structural R and α on output pose accuracy is analyzed, as shown in Figure 17 and Figure 18.

Through the analysis of the output pose error curves in Figure 17 and Figure 18, it can be observed that the changes of the structural parameters of the PM have the following effects on the output pose accuracy: Compared with the structural parameters α and β, the structural parameters R and R_0 have greater influence on the output pose accuracy. Except for a special position, the structural parameters α and β have little influence on the output pose accuracy; It can be found from Figure 19 that

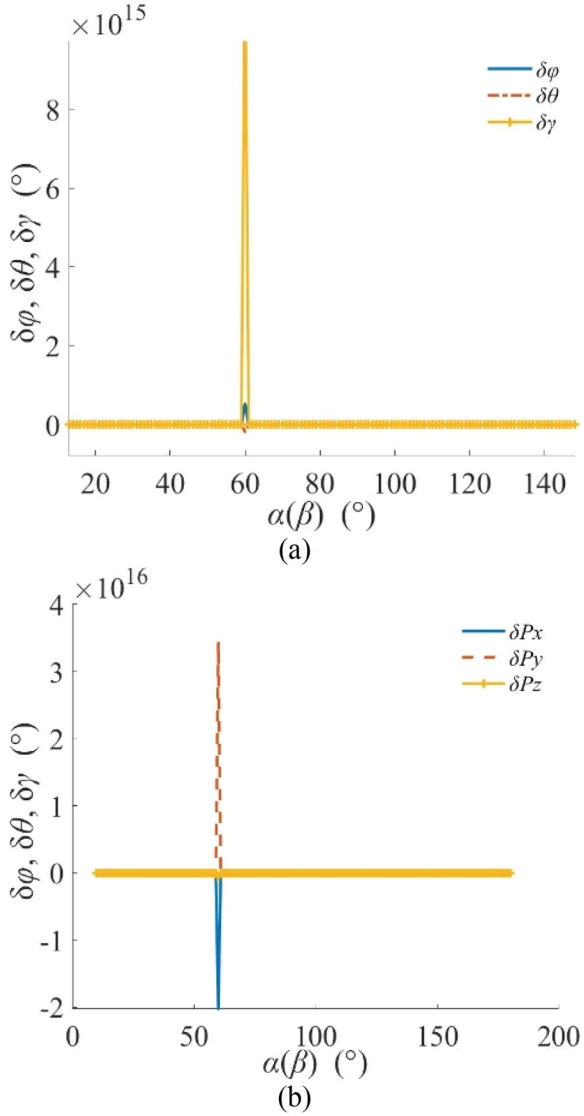

Figure 18 Relation between $\alpha(\beta)$ and output pose errors: **a** δP_x, δP_y, δP_z to $\alpha(\beta)$, **b** $\delta\varphi$, $\delta\theta$, $\delta\gamma$ to $\alpha(\beta)$

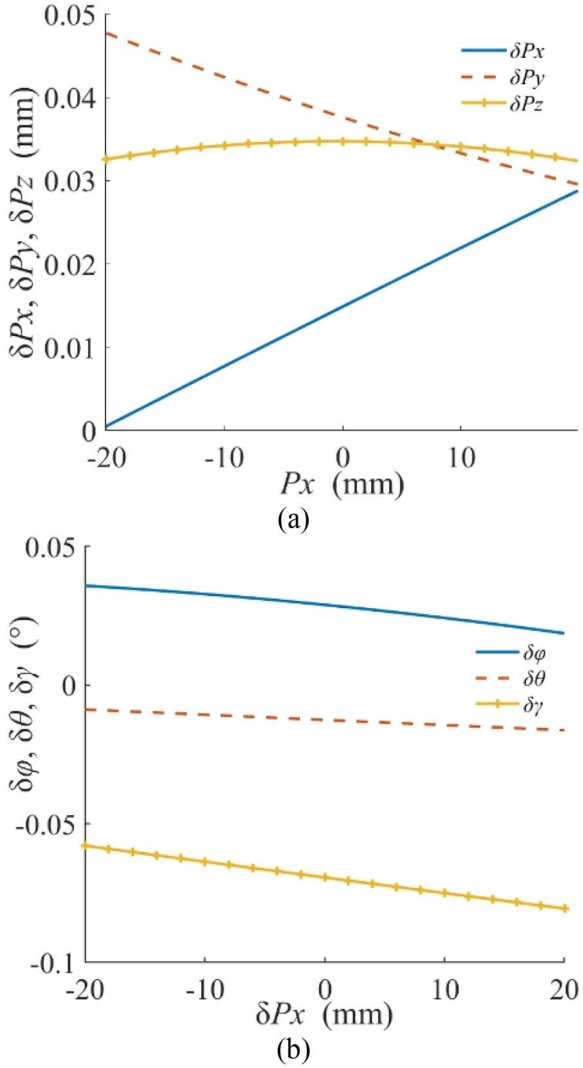

Figure 19 Relation between pose parameter P_x and output pose errors: **a** δP_x, δP_y, δP_z to P_x, **b** $\delta\varphi$, $\delta\theta$, $\delta\gamma$ to P_x

the influence of structural parameters R and R_0 on the accuracy of output pose tends to be flat with the increase of R and R_0.

It can be observed from Figure 19 and Figure 20 that when the pose parameter P_x and ϕ changes individually, the accuracy of the output pose changes as follows: The error dP_x in X-axis increases, as the pose parameter P_x increases from −20 mm to 20 mm; The errors dP_y in Y-axis and the error $d\phi$ of pose angle ϕ decrease with the increase of pose parameters; The error dP_z in Z-axis increases at early stage and then decreases with the increase of parameters P_x, and reaches the maximum at P_x=0. The error $d\theta$ and $d\gamma$ increases with the increase of P_x, and the absolute value of them increases constantly.

As the pose parameter ϕ increases, the error dP_x in X-axis direction, the errors dP_y in Y-axis and the error $d\phi$ of pose angle ϕ increase simultaneously; The error dP_z in Z-axis increases decreases with the increase of parameters ϕ; The error $d\theta$ and $d\gamma$ increases with the increase of ϕ, and the absolute value of them increases constantly. The overall output pose error indicates an increasing trend as the pose angle ϕ increases constantly.

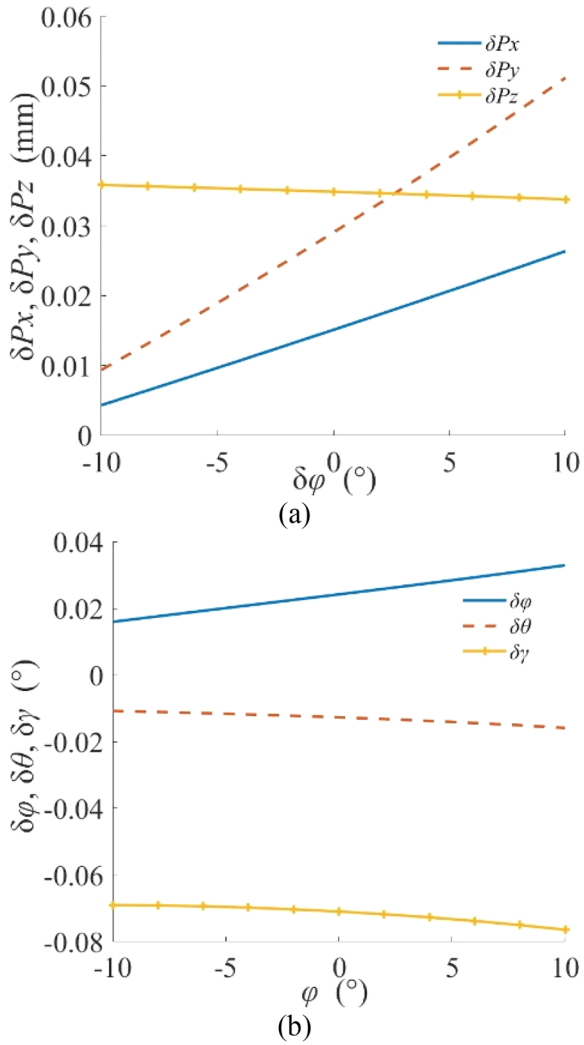

Figure 20 Relation between pose parameter φ and output pose errors: **a** δP_x, δP_y, δP_z to φ, **b** $\delta\varphi$, $\delta\theta$, $\delta\gamma$ to φ

5 Conclusions

(1) A novel 6-UCU bone-attached PM is proposed. It has the characteristics of compact structure, high accuracy, large bearing capacity and six-axis force feedback, which can meet the needs of bone-attached operation. The height of the PM is only 120 mm in initial state, and the radiuses of the moving platform and the fixed base are 50 mm.

(2) The factors, the length of the link, the rotation angle of the joint and the interference between the components, that affect the workspace are analyzed. Based on that factors, the workspace model of the 6-UCU PM is established by using the method of spherical coordinate search. And the influence of structural parameters on the robot's workspace is analyzed. The analysis result can improve the design efficiency and ensure that the robot has a small mechanical size possesses a large workspace.

(3) An error modeling method is developed based on the structure of 6-UCU PMs. According to the established error model, the output pose error curve is drawn by using MATLAB software when the structure parameters change, and the influence of the structure and pose parameters change on the output pose error of PMs is analyzed. In addition, the method can also be further applied to the accuracy analysis of other PMs.

Acknowledgements
Not applicable.

Authors' contributions
DL and HW was in charge of the whole trial; KD and CX wrote the manuscript; XX and XG assisted with analyses and simulation. All authors read and approved the final manuscript.

Authors' Information
Kaijie Dong, born in 1989, is currently a PhD candidate at *School of Automation, Beijing University of Post and Telecommunications, China*. He received his bachelor degree from *China Agricultural University, China*, in 2013. His research interests include deployable mechanism and robotics. E-mail: dongkaijiedj@163.com.
Duanling Li, born in 1974, is currently a professor at *School of Automation, Beijing University of Post and Telecommunications, China*. She received her PhD degree from *Beihang University, China*. Her research interests include metamorphic mechanism, mechachonics engineering and robotics. E-mail: liduanling_bupt@163.com.
Xingyu Xue, born in 1997, is currently a master candidate at *School of Automation, Beijing University of Post and Telecommunications*, China. He received his bachelor degree from *Beijing University of Post and Telecommunications, China*, in 2020. His research interests include metamorphic mechanism and robotics.
Chang Xu, born in 1994, is currently a junior engineer at *the 38th Research Institute of China Electronics Technology Group Corporation, China*. He received his master degree from *Beijing University of Post and Telecommunications, China*.
Haowei Wang, born in 1987, is currently a senior engineer at *China Academy of Space Technology*. He received his master degree from *Harbin Institute of Technology, China*. His research interests include high precision mechanism and applications. E-mail: wanghaowei000@126.com.
Xianming Gao, born in 1984, is currently working at *Shannxi University of Science and Technology, China*. His research interests include simulation of heat and structural optimization method.

Funding
Supported by National Natural Science Foundation of China (Grant Nos. 51775052, 52175019), Beijing Municipal Natural Science Foundation of China (Grant No. 21C10109) and Beijing Municipal Key Laboratory of Space-ground Interconnection and Convergence of China.

Availability of data and materials
All data and materials generated or analysed during this study are included in this published article.

Competing Interests
The authors declare no competing financial interests.

Author Details
[1]School of Automation, Beijing University of Posts and Telecommunications, Beijing 100876, China. [2]38th Research Institute of China Electronics Technology Group Corporation, Hefei 340100, China. [3]Beijing Institute of Spacecraft System Engineering, China Academy of Space Technology, Beijing 100094, China. [4]College of Mechanical and Electrical Engineering, Shaanxi University of Science and Technology, Xi'an 712000, China.

Received: 28 May 2021 Revised: 24 December 2021 Accepted: 4 February 2022
Published online: 06 April 2022

References

[1] Z Huang, L F Kong. *Mechanism theory and control of parallel manipulator*. Beijing: China Machine Press, 1997. (in Chinese)
[2] J A Koenig, C Plaskos. *Total knee arthroplasty technique: OMNIBotics*. Berlin: Springer, 2019: 167-183.
[3] Y Liu, L Q Sun, Y B Fan. Overview and development of orthopedic robot. *China Medical Devices*, 2021, 36(1): 159-163. (in Chinese)
[4] T Ginoya, Y Maddahi, K Zareinia. A historical review of medical robotic platforms. *Journal of Robotics*, 2021. https://doi.org/10.1155/2021/6640031.
[5] L T Yan, Q Wang, H Y Wang, et al. Review of continue surgical robot actuated by SMA. *Journal of Mechanical Engineering*, 2021, 57(11): 138-152. (in Chinese)
[6] S Bahadori, T W Wainwright, P Subramanian, et al. A review of the evolution of robotic-assisted total hip arthroplasty. *Hip International: the Journal of Clinical and Experimental Research on Hip Pathology and Therapy*, 2019, 29(3): 232-238.
[7] J Douissard, M E Hagen, P Morel. The Da Vinci Surgical System. *Bariatric Robotic Surgery*, Cham: Springer, 2019: 13-27.
[8] X Wu, J Q Wang, X Sun, et al. Guidance for the treatment of femoral neck fracture with precise minimally invasive internal fixation based on the orthopaedic surgery robot positioning system. *Orthopaedic Surgery*, 2019, 11(3): 335-340.
[9] J Q Wang, Y B Fan. Results of treatment for femoral neck fracture will be improved by computer assisted orthopaedic surgery. *China Journal of Orthopaedics and Traumatology*, 2018, 31(2): 99-102. (in Chinese)
[10] P Kazanzides, B D Mittlelstadt, B L Musits, et al. An integrated system for cementless hip replacement. *IEEE Engineering in Medicine and Biology*, 1995: 307–313.
[11] J P Merlet. *Parallel robots*. 2nd ed. Dordrecht: Springer, 2006.
[12] B L Davies, K L Fan, R D Hibberd, et al. ACROBOT-using Robots and surgeons synergistically in knee surgery. *Proceedings of the 8th IEEE International Conference on Advanced Robotics*, 1997: 173-178.
[13] M Jakopec, S J Harris, Baena F, et al. The Acrobot system for total knee replacement. *Industrial Robot*, 2003, 30(1): 61-66.
[14] A Wolf, M Shohan, S Michael, et al. Morphometric study of the human lumbar spine for operation-workspace specifications. *Spine*, 2001, 26(22): 2472-2477.
[15] A Wolf, M Shohan, S Michael, et al. Feasibility study of a mini, bone-attached, robotic system for spinal operation. *Spine*, 2004, 29(2): 220-228.
[16] L Pransky. The Pransky interview: Professor Moshe Shoham, Founder of Mazor Robotics and Microbot Medical. *Industrial Robot: An International Journal*, 2014, 41(5): 393–397.
[17] B Fiani, S A Quadri, M Farooqui, et al. Impact of robot-assisted spine surgery on health care quality and neurosurgical economics: A systemic review. *Neurosurgical Review*, 2020, 43: 17–25.
[18] B Jiang, T D Azad, E Cottrill, et al. New spinal robotic technologies. *Frontiers of Medicine*, 2019, 13: 723–729.
[19] J Zhang, Y Q Zhao, J S Dai. Compliance modeling and analysis of a 3-RPS parallel kinematic machine module. *Chinese Journal of Mechanical Engineering*, 2014, 27(4): 703—713.
[20] K A Arrouk, B C Bouzgarrou, G Gogu. CAD based geometric procedures for workspace and singularity determination of the 3-RPR parallel manipulator. *Applied Mechanics and Materials*, 2012, 162: 131-140.
[21] H Xiong, X M Diao. Geometric isotropy indices for workspace analysis of parallel manipulators. *Mechanism and Machine Theory*, 2018(128): 648-662.
[22] J Fu, F Gao. Optimal Design of a 3-Leg 6-DOF parallel manipulator for a specific workspace. *Chinese Journal of Mechanical Engineering*, 2016, 30(4): 659-668.
[23] A Antonov, V Glazunov. Position, velocity, and workspace analysis of a novel 6-DOF parallel manipulator with "piercing" rods. *Mechanism and Machine Theory*, 2021, 161: 104300.
[24] Y D Xu, D S Zhang, M Wang, et al. Type synthesis of Two-Degrees-of-Freedom rotational parallel mechanism with two continuous rotational axes. *Chinese Journal of Mechanical Engineering*, 2016, 29(4): 694—702.
[25] T Sun, S F Yang, B B Lian. *Finite and Instantaneous screw theory in robotic mechanism*. Singapore: Springer, 2020.
[26] C Xu. Structure design and application of small 6-DOF parallel robot. *Beijing: Beijing University of Post and Telecommunications*, 2019. (in Chinese)
[27] Z H Zhan, X M Zhang, Z C Jian, et al. Error modelling and motion reliability analysis of a planar parallel manipulator with multiple uncertainties. *Mechanism and Machine Theory*, 2018, 124: 55-72.
[28] X H Zhao, Q Q Luan, L Zhao, et al. Kinematics modeling and error analysis of 3-RRRU parallel manipulator. *Machinery Design & Manufacture*, 2020, 01: 274-276,280. (in Chinese)
[29] N Wang, T Zhang, Q H Wang. Kinematics error modeling and verification of 3UPS-PU parallel mechanism. *Journal of Mechanical Transmission*, 2020, 44(07): 113-118. (in Chinese)
[30] T Sun, Y M Song, Y G Li, et al. Separation of comprehensive geometrical errors of a 3-DOF PM based on Jacobian matrix and its sensitivity analysis with Monte-Carlo method. *Chinese Journal of Mechanical Engineering*, 2011, 24(3): 406-413.